

# AI-based association analysis for medical imaging using latent-space geometric confounder correction

Xianjing Liu<sup>1,2\*</sup>, Bo Li<sup>1\*</sup>, Meike W. Vernooij<sup>1,3</sup>, Eppo B. Wolvius<sup>2</sup>, Gennady V. Roshchupkin<sup>1,3#</sup>, Esther E. Bron<sup>1#</sup>

<sup>1</sup>Dept. of Radiology & Nuclear Medicine, Erasmus University Medical Center, Rotterdam, the Netherlands

<sup>2</sup>Dept. of Oral and Maxillofacial Surgery, Erasmus University Medical Center, Rotterdam, the Netherlands

<sup>3</sup>Dept. of Epidemiology, Erasmus University Medical Center, Rotterdam, the Netherlands

\*,# These authors contributed equally to this work.

## Abstract

AI has greatly enhanced medical image analysis, yet its use in epidemiological population imaging studies remains limited due to visualization challenges in non-linear models and lack of confounder control. Addressing this, we introduce an AI method emphasizing semantic feature interpretation and resilience against multiple confounders. Our approach's merits are tested in three scenarios: extracting confounder-free features from a 2D synthetic dataset; examining the association between prenatal alcohol exposure and children's facial shapes using 3D mesh data; exploring the relationship between global cognition and brain images with a 3D MRI dataset.

Results confirm our method effectively reduces confounder influences, establishing less confounded associations. Additionally, it provides a unique visual representation, highlighting specific image alterations due to identified correlations.

Keywords: Artificial Intelligence, epidemiology, association analysis, confounder, interpretability

## Introduction

Artificial intelligence (AI) has arisen as a powerful asset across various domains, largely due to its capacity to identify discriminative patterns within high-dimensional data sets. This capacity has been particularly useful in the realm of medical imaging analysis, where AI techniques have proven successful for diagnostic and prognostic prediction tasks [30]. However, the application of AI in medical imaging-based association analysis for epidemiological studies has met with certain challenges. These include deriving clinically or epidemiologically significant insights from AI-generated results, a task which, when compared to traditional statistical methods, has proven difficult [31,58]. This is primarily due to two factors: the complexity of visualizing non-linear modeling in AI models, which is also known as the "black box" issue; and the lack of control over confounding variables. These hurdles highlight the need for more interpretable and confounder-free AI models in epidemiological applications.

To overcome the complexity of visualizing non-linear modeling, several feature interpretation and visualization techniques have been developed to provide a deeper understanding of outcome associations. In medical imaging research field, these techniques generally fall into two main categories [32]. The first category encompasses gradient and backpropagation methods, which typically examine the gradients or activations within the AI model, creating a heatmap linked to an input image. This heatmap highlights the regions that are most influential to the predicted outcome. Example methods include Gradient-weighted Class Activation Mapping (Grad-CAM) [33], SHAP [34], DeepTaylor [35], and Layer-wise backpropagation [36]. The second category involves reconstruction and generative methods [19,24,37,38,39]. These methods manipulate the latent space of generative models, and reconstruct from it a sequence of images that illustrate how a specific attribute (e.g., age) is associated with the changes of these images [39]. Together, these two categories of techniques offer valuable insights into the workings of AI models, supporting their interpretability in medical applications.

A confounder is a variable that simultaneously affects both the independent and dependent variables in an association analysis [1,2]. Consequently, it can falsely create, amplify, or reduce an association between these variables. For example, in a study investigating the association between disease severity (independent variable) and patient recovery time (dependent variable), the patient's overall health status could serve as a confounder, since both disease severity and recovery time could be influenced by the patient's health status. Therefore, without controlling for this confounder, AI models predicting recovery time might inadvertently factor in features related to the overall health status. And these features in turn will confound the outcome, obscuring the influence of disease severity alone on recovery time. Although this confounding problem is well-known in classical epidemiological studies, the field of AI provides limited methodology to correct for confounders. Furthermore, this issue becomes exacerbated in scenarios with multiple confounders, making the development of confounder-free AI models essential.

To mitigate confounding issues in AI methods, several approaches have been proposed, such as adversarial training [9,10,11,12], disentanglement [13,14,15,42,43], and metadata normalization (MDN) [40,41]. The adversarial training approaches train neural networks to predict the confounder variable from the learned features, and subsequently to minimize the prediction performance in order to remove confounding information from the latent features. Alternatively, disentanglement approaches train neural networks to minimize the dependency between the latent features and the confounder using an additional loss term

that measures their mutual Information [14] or maximum mean discrepancy [13]. Lastly, the MDN approach inserts a special layer into neural networks. This layer is designed to regress out confounding information, allowing only residual signals to propagate to the subsequent layers of the network.

Despite the rapid advancements in AI, there currently exist no tailored AI methods for association analysis in medical imaging. The challenge lies in incorporating feature interpretation into AI methodologies while ensuring they remain free from confounder influences. Predominantly, the confounding issues within existing AI systems are addressed by eradicating confounding information from the latent features [9,10,11,12,13,14]. However, this approach risks diminishing the diversity of information contained within these latent features and ultimately impacting the image reconstruction quality in generative models, thereby constraining their potential applicability in feature visualization [19]. To address this, we look for a different strategy and propose a new algorithm for image-based association analysis that enables feature interpretation and confounder correction. We consider the latent space of an autoencoder as a vector space, where most imaging-related variables (e.g., a learning target  $\mathbf{t}$  and a confounder  $\mathbf{c}$ ) have a vector direction that captures their variability [24]. Then the confounding issues are solved by determining a confounder-free vector which is orthogonal to  $\vec{c}$  but as collinear to  $\vec{t}$  as possible (Fig. 1(a)). Afterwards, we interpret the learned features by sampling and reconstructing images along the confounder-free vector. We demonstrate the performance of the proposed approach and its value in three applications with either synthetic images or real medical images in a population-based research setting, and with a focus on the proposed semi-supervised learning that utilizes unlabeled imaging data.

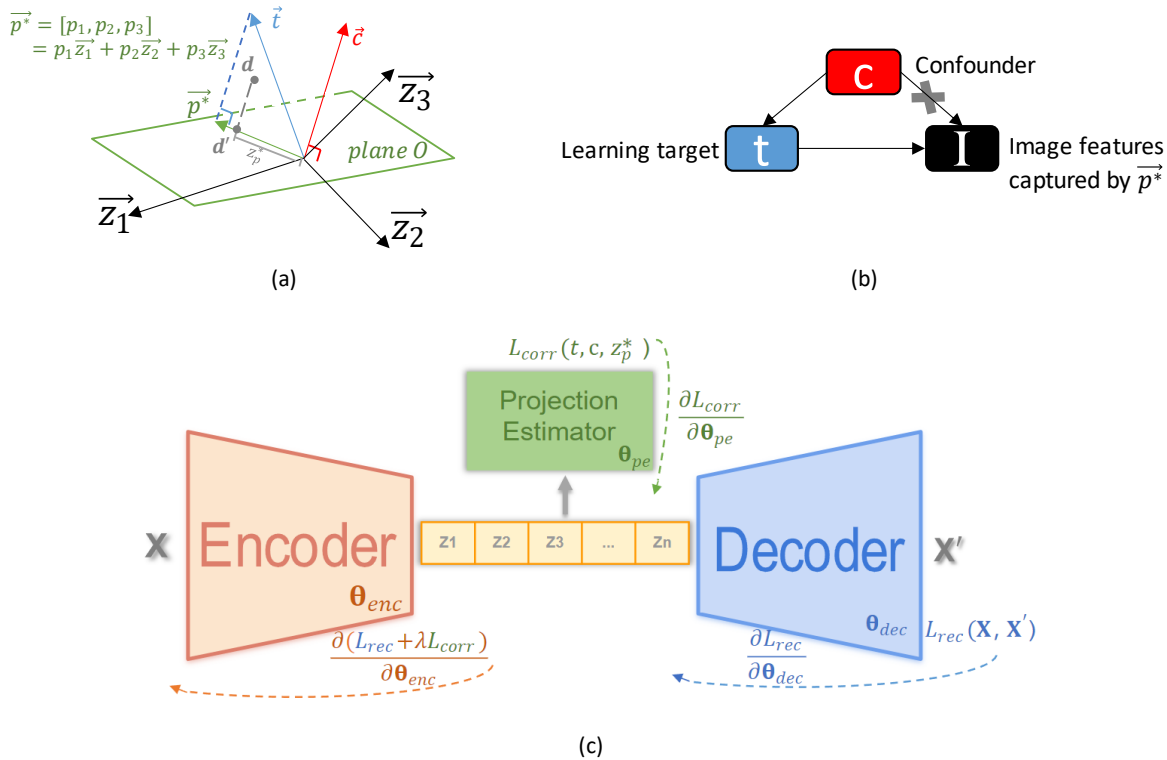


**Fig. 1:** The proposed AI approach for association analysis in medical imaging. **(a)** Geometry perspective of correlations between a target and a confounder variable ( $\mathbf{t}$ ,  $\mathbf{c}$ ), and its extension ( $\vec{t}$ ,  $\vec{c}$ ) into the latent space ( $n=3$  latent dimensions) of an autoencoder. Plane  $O$  is orthogonal to  $\vec{c}$ .  $\vec{p}^*$  is the vector projection of  $\vec{t}$  onto plane  $O$ .  $\mathbf{d}$  is the latent representation of an input image and  $\mathbf{d}'$

is its projection onto  $\overline{p^*}$ .  $z_p^*$  is the distance between  $\mathbf{d}'$  and the origin. For cases with  $m$  confounders, the latent dimensions should be  $n \geq m + 1$ , so as to guarantee there exist a  $\overline{p^*}$  orthogonal to  $m$  confounders; **(b)** a directed acyclic diagram explains the relationships between  $\mathbf{t}$ ,  $\mathbf{c}$ , and image  $I$ . We aim to extract image features associated with the learning target while being independent to the confounders. **(c)** The proposed approach in a neural network perspective.  $[z_1, z_2, \dots, z_n]$  are the learned latent features by the network, which construct the latent space shown in (a).  $\mathbf{X}$  and  $\mathbf{X}'$  refer to the input and reconstructed image, by reconstructing the image, its latent features are extracted.  $\theta_{enc}$ ,  $\theta_{dec}$ ,  $\theta_{pe}$  are the trainable parameters of encoder, decoder, and projection estimator.

## Experiments and Results

### *Overview of the proposed methods.*

The proposed method consists of three steps. First, an autoencoder, including an encoder and a decoder, is trained to construct compact representations of input images in a latent space (Fig. 1(c)). Second, we consider the latent space of this autoencoder to be a vector space, where the Pearson’s correlation between target and confounder variables ( $\mathbf{t}$  and  $\mathbf{c}$ ) is equivalent to the cosine value between the vectors ( $\cos\langle\vec{t}, \vec{c}\rangle$ ) [17, 18]. Next, we narrow down the confounder mitigation problem into searching a vector  $\vec{p}^*$  in the latent space that is orthogonal to  $\vec{c}$  while still being as close to  $\vec{t}$  as possible (Fig. 1(a)). We solve this orthogonalization problem using a novel statistics-based correlation loss, which not only performs vector searching in the latent space, but enforces the encoder (Fig. 1(c)) to generate latent features with linear correlation to  $\mathbf{t}$  and  $\mathbf{c}$ . Third, we visualize the established correlation using the decoder. A sequence of images is reconstructed by decoding latent features sampled along the vector  $\vec{p}^*$  in the latent space, showing changes associated with the learning target while being maximally independent from the confounders.

We demonstrate the performance of the proposed approach in three applications using 2D synthetic, 3D facial mesh, and 3D brain imaging data, and showing the use of 2D convolutional autoencoder [44], 3D graph convolutional autoencoder [45], and 3D convolutional autoencoder [25] within our architecture-agnostic framework. For all three experiments, we applied 5-fold cross-validation and ensured that repeated scans from the same subject were in the same training or validation set.

### *3.1 Synthetic data*

In the first experiment, we construct a synthetic dataset to facilitate the understanding of the confounding problem as well as the proposed solution. The dataset (section 2.1, Fig. S1, Fig. 2) consists of 2D grayscale images of solid circles with different brightness and radius, in which a larger radius is strongly correlated with a lower brightness. Brightness is used as the learning target and the circle radius is used as a confounder. Given that the input images can be represented by two features (brightness and radius), a latent space with two dimensions would be sufficient to fully reconstruct the input images (Fig. 2). We thus set the latent dimension of this autoencoder to be two. We quantify the performance of prediction accuracy by the root mean square error (r-MSE) between the target and the predicted brightness, the reconstruction quality by the mean  $L1$ -norm between the input and reconstructed images, and the confounding correction by the Pearson’s correlation coefficient between the latent image representation ( $\mathbf{z}_p$ ) and the confounder variable of radius (Table 1).

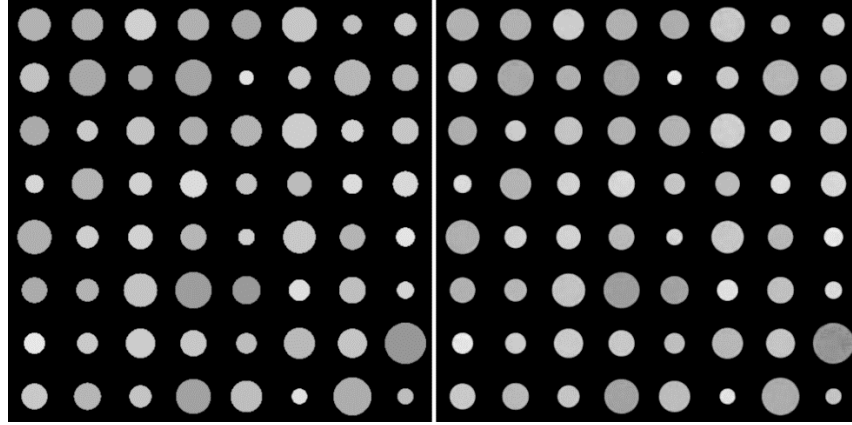


**Fig.2:** The input images  $X$  (64 images on the left) and reconstructed images  $X'$  (64 image on the right) from the autoencoder.

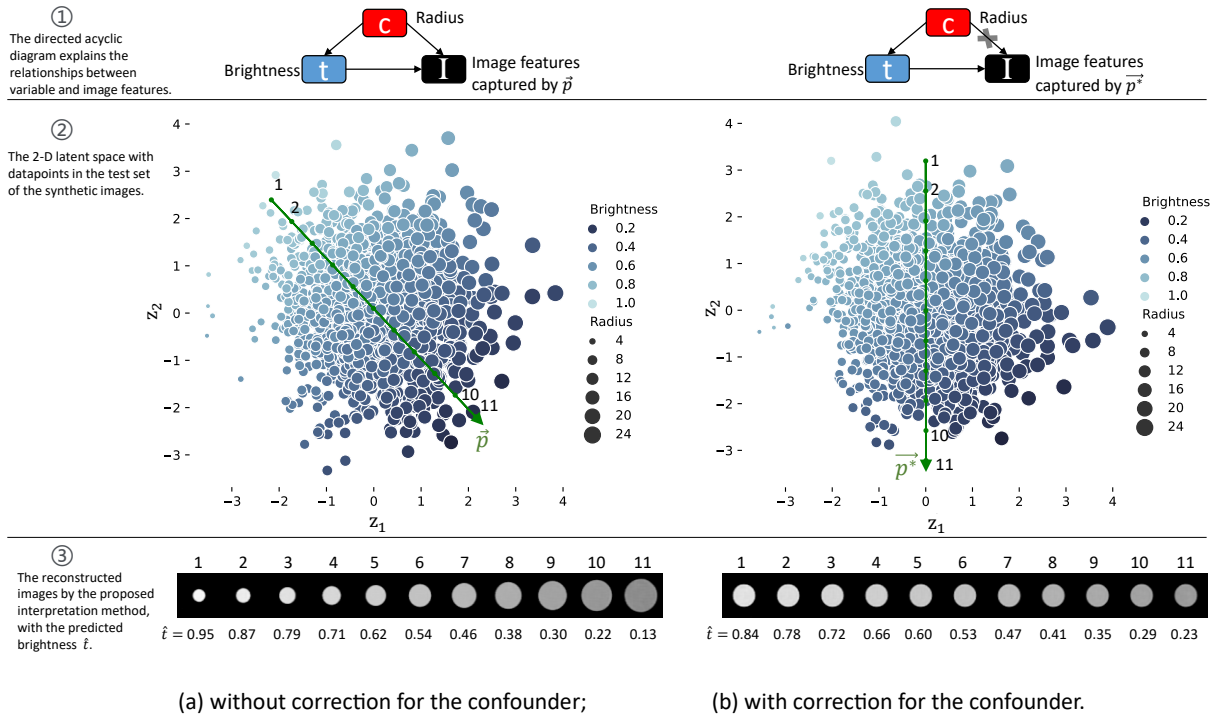


**Fig 3:** The distribution of the 2-D latent space for the synthetic images in the test set of Experiment 1, and the eleven reconstructed images sampling along the brightness-related vector, (a) without (i.e., vector  $\vec{p}$ ) and (b) with correction (vector  $\vec{p}^*$ ) for the confounding of circle radius, together with the predicted brightness  $\hat{t}$  (Eq. 6 and Eq. 7).  $Z_1$ -axis: the first dimension of the latent space;  $Z_2$ -axis: the second dimension. Each data point in the latent space represents an input image, which is denoted by its radius and brightness. After training, eleven frames were reconstructed by sampling eleven points along the vector  $\vec{p}$  and  $\vec{p}^*$  (Eq. 6, Eq. 7) to visualize the confounding effects.

**Table 1:** Prediction error, Pearson's correlation coefficient, and image reconstruction quality of the methods without (NA) and with (\*) correction for the circle radius (confounder) in predicting the circle brightness (learning target) on the test set. A better performance is indicated by a bold value.

Confounder correction	Prediction error	Pearson’s correlation coefficient		Image reconstruction
	r-MSE (brightness)	$r(\mathbf{z}_p, \text{brightness})$	$r(\mathbf{z}_p, \text{radius})$	L1-norm
NA	<b>0.018±0.003</b>	<b>-0.991±0.003</b>	+0.670±0.024-	<b>0.008±0.001</b>
*	0.096±0.004	-0.737±0.011	<b>+0.026±0.006</b>	0.009±0.002

‘+’ and ‘-’ indicates a positive or negative correlation between  $\mathbf{z}_p$  and the variables.

We plot all 2D latent representations of the test set images, together with the estimated target variable-related vector (confounder-free vector  $\vec{p}^*$ , confounded vector  $\vec{p}$ ; Fig. 3). Fig. 3 shows that the variability of both brightness and radius variable are linearly encoded in the latent space following the supervision of the correlation loss (Eq. 5). Without adjusting for the circle radius (Fig. 3(a)), vector  $\vec{p}$  effectively captured the variation in the circle brightness - as indicated by the high correlation of  $r(\mathbf{z}_p, \text{brightness}) = -0.991$  presented in Table 1 – demonstrating exceptional prediction accuracy. However, sampling along vector  $\vec{p}$  in the 2D latent space not only moved towards data points with a lower brightness but also those with a larger radius (see Fig. 3(a)), suggesting a prominent confounding problem. This confounding issue was similarly revealed by the proposed feature interpretation method. When we reconstruct images with decreasing brightness based on the identified association, there was a noticeable increase in the circle’s radius (Fig. 3(a)③), because vector  $\vec{p}$  also partially captured the variability of the radius ( $r(\mathbf{z}_p, \text{radius}) = +0.670$  in Table 1).

On the contrary, when employing the proposed confounder correction, vector  $\vec{p}^*$  still captured the brightness variance, but remained almost unaffected by the change in the radius (Table 1;  $r(\mathbf{z}_p^*, \text{brightness}) = -0.737$ ,  $r(\mathbf{z}_p^*, \text{radius}) = +0.026$ ). Sampling along vector  $\vec{p}^*$  in the latent space led to data points with a lower brightness, but there were no discernible changes in the radius (Fig. 3(b)). Similarly, the proposed interpretation method showed that when images were reconstructed with decreasing brightness based on the established confounder-free association, the circle radius visually remained constant (Fig. 3(b)③).

In this synthetic dataset, the Pearson’s correlation between circle radius and brightness ( $r(\mathbf{t}, \mathbf{c})$ ), is 0.668 (section 2.1, Fig. S1). Theoretically, after fully adjusting for the confounder, the upper bound (as defined in Eq. 1) of any remaining correlation between  $\mathbf{z}_p^*$  and the learning target should be  $|r(\mathbf{z}_p^*, \mathbf{t})| \leq \sqrt{1 - r^2(\mathbf{t}, \mathbf{c})} = 0.744$ , subject to  $r(\mathbf{z}_p^*, \mathbf{c}) = 0$ . This theoretical upper bound is in line with our observed result of  $|r(\mathbf{z}_p^*, \text{brightness})| = 0.737$ , with  $r(\mathbf{z}_p^*, \text{radius}) = 0.026$  (Table 1). Furthermore, when we compared our approach with an existing adversarial learning-based confounder correction method (CF-Net [12]) in terms of the metrics specified in Table 1, we found that both methods yielded similar outcomes (Table S1).

### 3.2 Alcohol exposure prediction from facial photos in children population

High levels of prenatal alcohol exposure (PAE) during pregnancy can have significant adverse effects on a child’s health development resulting in fetal alcohol spectrum disorder (FASD) with abnormal facial

development [46]. The association of low–moderate levels of PAE with the child’s facial development is less known. We thus applied the proposed method with multiple-confounder correction to study the associations between low-to-moderate prenatal alcohol exposure and children’s facial shape on a large population-based birth cohort (Generation R, [47]). We used maternal alcohol consumption as the learning target (PAE 1: drinking during pregnancy; PAE 0: not drinking), and as suggested by a previously similar study [51,55] using traditional statistical method with traditional confounder control, we used sex, ethnicity, BMI, maternal age, and maternal smoking during pregnancy as confounders, resulting in N=755 exposed and N=760 non-exposed samples. In addition, we included 3496 missing-label samples and focused on the semi-supervised learning (SSL) setting (**Algorithm 1** in supplementary). The results of fully supervised learning are provided in Table S3. The data characteristic is provided in Table 2, where maternal smoking ( $p < 0.001$ , two-sample t-test), maternal age ( $p < 0.001$ ), child BMI ( $p < 0.001$ ), and especially ethnicity ( $p = p < 0.001$ ) showed imbalanced distribution between the non-exposed and exposed groups.

**Table 2:** Data characteristic of children and their mothers included in the analysis (for the labeled data only, N=1,515).

Characteristic	Non-exposed (N=760)	Exposed (N=755)	Two sample t-test p-value
Child’s ethnicity, No. (%)			
1: Western	328 (43.2%)	670 (88.7%)	1.94e-87
0: Non-Western	432 (56.8%)	85 (11.3%)	
Child’s sex, No. (%)			
0: Male	357 (47.0%)	370 (49.0%)	0.44
1: Female	403 (53.0%)	385 (51.0%)	
Child’s BMI, mean $\pm$ SD	18.6 $\pm$ 3.2	16.8 $\pm$ 2.0	4.58e-37
Maternal smoking, No. (%)			
1: Yes	204 (26.8%)	417 (55.2%)	2.53e-30
0: No	556 (73.2%)	338 (44.8%)	
Maternal age, mean $\pm$ SD	28.2 $\pm$ 5.0	32.1 $\pm$ 3.9	8.60e-62

For binary prediction using the learned latent image features, the accuracy was quantified by the area under the receiver operating characteristic curve (AUC). As results shown in Table 3, when without correction for confounders, the Pearson’s correlation coefficient between facial image features ( $\mathbf{z}_p$ ) and PAE was +0.405, and the prediction AUC of PAE was at 0.746. The observed correlation coefficients between  $\mathbf{z}_p$  with ethnicity and BMI were +0.389 and -0.349, i.e., at a similar strength as that of the learning target PAE. The observed correlation coefficients for child sex, maternal smoking, and maternal age were +0.049, +0.180 and +0.216. After correcting for the confounders of ethnicity, BMI, sex, maternal smoking,



and maternal age using the proposed method, the correlation coefficient between facial image features ( $\mathbf{z}_p^*$ ) and PAE decreased to +0.156, which is higher than the correlation coefficient for the confounders (ethnicity: +0.064; BMI: -0.040; sex: +0.043; maternal smoking: +0.026; maternal age: +0.028).

**Table 3: Association analysis between PAE (learning target) and children’s facial shape (input image).** Results are presented without (NA) and with (\*) controlling of the confounders (ethnicity, BMI, sex, maternal smoking and maternal age), for the semi-supervised learning setting. The metrics for AUC and PAE are the higher the better, those for ethnicity, BMI, sex, maternal smoking, maternal age, and L1-norm are the lower the better. Better performance is indicated by a bold value.

Confounder correction	Prediction accuracy	Pearson’s correlation coefficient between $\mathbf{z}_p$ and:						Image reconstruction
	AUC (PAE)	PAE	Ethnicity	BMI	Sex	Maternal smoking	Maternal age	L1-norm
NA	<b>0.746±0.018</b>	<b>+0.405±0.043</b>	+0.389±0.085	- 0.349±0.010	+0.049±0.043	+0.080±0.054	+0.216±0.049	<b>0.294±0.017</b>
*	0.592±0.004	+0.156±0.008	<b>+0.064±0.018</b>	- <b>0.040±0.016</b>	<b>+0.043±0.030</b>	<b>+0.026±0.009</b>	<b>+0.028±0.026</b>	0.312±0.015

+’ and ‘-’ indicates a positive and negative correlation between  $\mathbf{z}_p$  and the variables.

We provide visual interpretation for the learned association without and with confounder correction (Fig. 4). In the setting without confounder correction, Fig. 4(a) indicates that PAE could lead to a narrow nasal bridge, deep-set eyes, and a narrow cheek. However, such detected facial features might not be the true association with PAE, because they were highly confounded by ethnicity and BMI ( $r(\mathbf{z}_p, \text{ethnicity}) = +0.310$  and  $r(\mathbf{z}_p, \text{BMI}) = -0.334$  in Table 3). Actually, a narrow nasal bridge and deep-set eyes are common facial features in the Western population [48, 49], while a narrow cheek is common in lower-BMI population [50]. After correcting for all confounders, these facial features were not observed in Fig. 4(b) anymore. This change suggests that the proposed method successfully removed facial features driven by the confounders, resulting in a confounder-free association between PAE and children’s facial shape. To provide more insights into the changes caused by each of the confounder variables, we apply the proposed feature interpretation method to visualize our confounder-free results with a gradually increased number of confounders to correct (Fig. 5, Eq. 4).

Our results suggest low to moderate maternal alcohol exposure during pregnancy is associated with children’s facial shape. Detected facial phenotypes included turned-up nose tip, shortened nose and turned-in lower-eyelid-related regions. These findings are consistent with previously similar studies [51], and in line with facial abnormality in fetal alcohol spectrum disorders [52] caused by high levels of PAE.

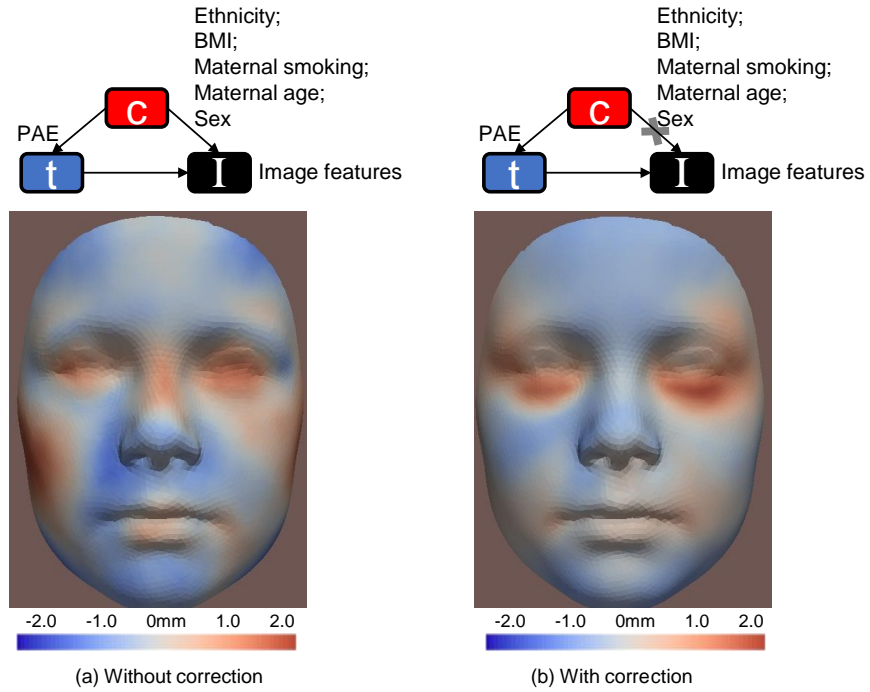


**Fig. 4:** Interpretation heatmaps of facial changes in children with PAE using the proposed method: **(a)** without correction for confounders; **(b)** with correction for ethnicity, BMI, maternal smoking, maternal age, and sex. Red areas refer to inward changes of the face with respect to the geometric center of the head. Heatmap generation is detailed in Section 2.2.3.

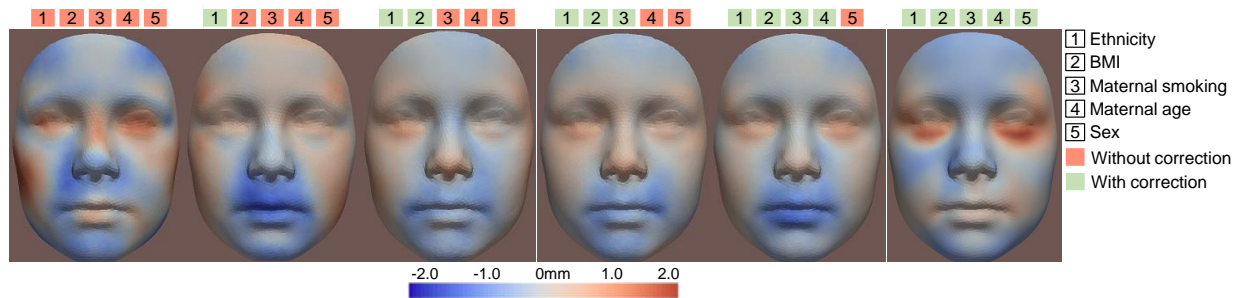


**Fig. 5:** Interpretation heatmaps of facial changes in children exposed to alcohol during pregnancy (PAE) using the proposed method with gradual correction for confounders of ethnicity, BMI, maternal smoking, maternal age, and sex. From left to right, in the first figure no confounder was corrected for during the training; in the last figure all five confounders were corrected (Eq. 4). Red areas refer to inward changes of the face with respect to the geometric center of the head.

### 3.3 Global cognition prediction from brain MRI in an elderly population

We applied the proposed method with multiple-confounder correction to study the associations between global cognition and brain imaging in a large elderly population (Rotterdam Study [26]). As

suggested by a previously similar study [58] using traditional statistical method with traditional confounder control, we used g-factor score [56] as learning target variable representing global cognition and used grey matter density maps as derived from T1-weighted brain MRIs as input images (section 2.1), and included age, sex, and educational years as confounders. The results show that age is a strong confounder in this study, i.e. participants with an older age generally have a lower g-factor score, (Fig. 6(a), p-value=4.88e-163). The detailed data characteristic of the study population is shown in Fig. 6. Similar as the previous experiment, in addition to labelled samples (N=2,395), we included missing-label samples (N=9,406) and focused on the semi-supervised learning. The results of fully supervised learning are provided in Table S4. We compared the findings with those obtained without confounder correction.

For the results without correcting for confounders, the correlation coefficient between brain imaging features ( $\mathbf{z}_p$ ) and g-factor was  $0.49 \pm 0.04$  (Table 4). Even though we explicitly maximized this correlation, it is still lower than the correlation coefficient with age ( $-0.73 \pm 0.01$ ). The observed correlation coefficients for sex and educational years were  $-0.08 \pm 0.03$  and  $+0.13 \pm 0.05$ , lower than that with age. For the results with correction for the confounders of age, sex, and educational years, the correlation coefficient between the brain image features ( $\mathbf{z}_p^*$ ) with g-factor decreased to  $+0.05 \pm 0.04$ , which is much lower than that without confounder correction. On the other hand, the correlation coefficients with the confounders were corrected into a similarly low level, ranged from 0.03 to 0.06. Notably, the image reconstruction quality as measured by the L1-norm and normalized cross-correlation remained similarly good after removing confounder-related information from brain image features, suggesting that with the proposed semi-supervised learning the confounder-free image features still contained essential information to reconstruct the brain morphometry at a high-resolution.

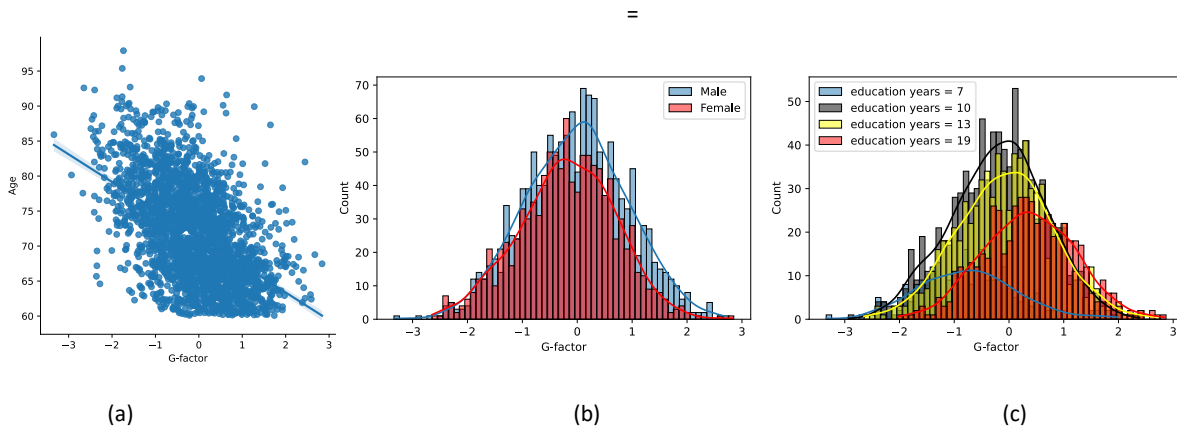


**Fig. 6:** Data characteristic of the study population. **(a)** Joint distribution of g-factor and age. The Pearson’s correlation coefficient between age and g-factor is  $-0.51$  (p-value =  $4.88e-163$ , linear regression); **(b)** Histogram distribution of g-factor between male and female. Male show slightly higher g-factor than female (p-value =  $1.4e-5$ , linear regression); **(c)** Histogram distribution of g-factor for different educational years. Higher educational years show overall higher g-factors (p-value =  $2.87e-57$ , linear regression).

**Table 4: Association analysis of the learning target global cognition (g-factor) and constructed brain features from grey matter density map ( $\mathbf{z}_p$ ).** Results are presented without (NA) and with (\*) controlling of confounders (age, sex, and educational years),

and for semi-supervised learning setting. The metrics for g-factor and normalized cross-correlation (NCC) are the higher the better, those for age, sex, educational years, and L1-norm are the lower the better. A better performance is indicated by a bold value.

Confounder correction	Prediction error	Pearson's correlation coefficient between $z_p$ and:				Image reconstruction	
	r-MSE (G-factor)	G-factor	Age	Sex	Educational years	NCC	L1-norm
NA	<b>0.80</b> ± <b>0.01</b>	<b>+0.49</b> ± <b>0.04</b>	-0.73 ± 0.01	-0.08 ± 0.03	+0.13 ± 0.05	0.22 ± 0.0008	0.09 ± 0.0003
*	0.91 ± 0.02	+0.05 ± 0.04	<b>-0.04</b> ± <b>0.03</b>	<b>-0.03</b> ± <b>0.02</b>	<b>+0.06</b> ± <b>0.04</b>	0.22 ± 0.0010	0.09 ± 0.0004

+ and - indicates a positive or negative correlation between  $z_p$  and the variables.

To visualize the anatomical regions purely linked with global cognition, while independent of age, sex, and educational years, we reconstructed brain grey matter maps from the obtained confounder-free image features (Fig. 7). Only statistically significant results ( $p < 0.05$ , paired t-test) were visualized, averaging results over five folds. Without confounder correction (Fig. 7(a)), the brain heatmaps showed widespread increases in grey matter density with an increasing g-factor, primarily in the cortex, thalamus, and hippocampus. After correcting for the confounding effects of age, sex, and educational years (Fig. 7(b)), the highlighted regions were mainly confined to the hippocampus and superior parietal gyrus, indicating a direct association with global cognition. Notably, regions like the left thalamus, initially showing a strong correlation, changed to zero, suggesting a stronger association with confounding variables such as age.

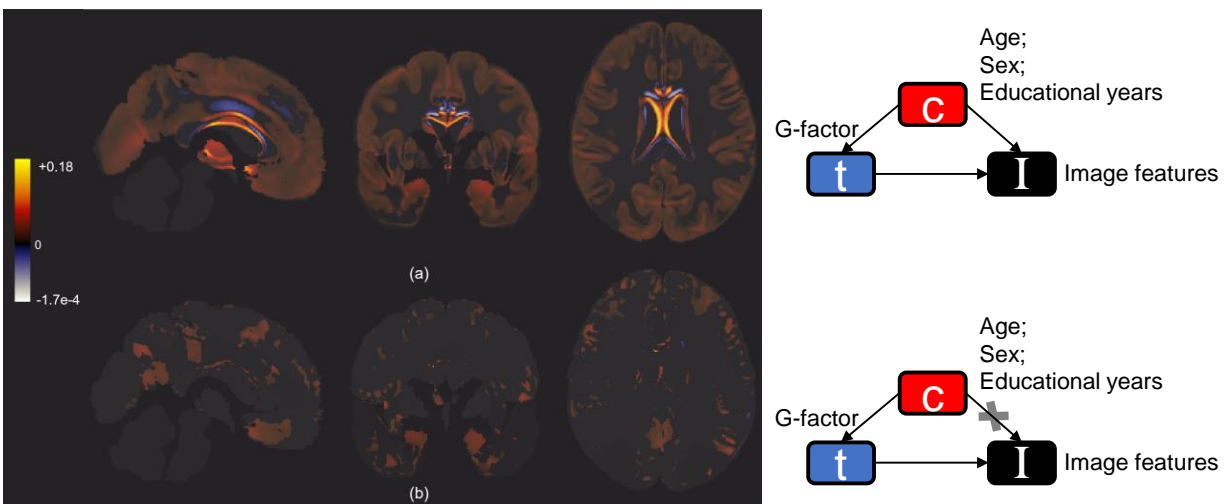


**Fig. 7:** Reconstructed supratentorial modulated grey matter maps using the sampled latent features along the direction of increasing g-factor **(a)** without correcting for confounders, and **(b)** with correcting for age, sex, and educational years. The results are generated using the semi-supervised model, averaged over the five folds, and masked out the statistically non-significant region. Color bar shows the direction and magnitude of the changes of GM density.

## Discussion

In this study, a novel AI method was proposed for conducting association analysis in medical imaging. Our proposed approach effectively addresses the influence of confounding factors by incorporating them as priors, resulting in confounder-free associations. To enhance the interpretability of the outcome associations, a semantic feature visualization approach was proposed, allowing us to gain valuable insights into the image features underlying the observed associations. Moreover, the proposed method supports semi-supervised learning, enabling use of missing-label image data.

The efficacy and generalizability of the proposed method were demonstrated in three experiments. In section 3.1, a synthetic circle dataset was constructed to facilitate the understanding of how the proposed methods handles confounders, with the goal to extract image features associated with circle brightness while not being confounded by circle radius. The proposed method successfully corrected for the confounder and obtained a remaining correlation of 0.737 (Table 1), which was very close the theoretical upper bound of 0.744 (Eq., 1). Furthermore, we also compared our approach with an existing adversarial learning-based confounder correction method (CF-Net [12]) in terms of the metrics specified in Table 1, and found that both methods yielded similar outcomes (Table S1). Afterwards, the proposed method was applied to two epidemiological association studies. In section 3.2, we analyzed the association between low-moderate prenatal alcohol exposure (PAE) and children's facial shape after correction for confounders, the proposed method removed facial features related to the confounders (e.g., a narrow cheek or deep-set eyes) and found a remaining correlation of 0.156 between facial features and PAE. In contrast, in section 3.3, the analysis of association between brain images and cognitive scores, almost no remaining association (Pearson correlation coefficient  $r = 0.05 \pm 0.04$  in Table 4) was found after the correction of confounders. It turned out that the strong association ( $r = 0.49 \pm 0.04$  in Table 4) between brain imaging and cognitions before the correction was mainly contributed by the age confounder. As these two applications demonstrate, confounder correction is essential as it may prevent wrong of misleading association results. This further highlights the importance of correcting for confounders in AI-based medical image analysis.

The proposed visualization approach highlights the features that drive the association, both in the analysis with and without correction for confounders. As demonstrated in section 3.1, the feature visualization was implemented by generating a sequence of images showing how features were changing associated with the learning target. One advantage of such an approach is that it not only highlights image regions contributing to the association, but also illustrate the direction (positive or negative) of the association. For example, in section 3.2 (Fig. 4) before correcting for the confounders (88.7% of the exposed children were Western), the facial heatmap highlighted the eyes regions, but also indicated they were moving inward. This direction information provides another evidence that such facial image features were confounded by ethnicity, because deep-set eyes is a common facial feature in the Western population [48]. Another advantage is that our approach for feature visualization linearly maps the magnitude of changes in image features with the magnitude of changes in the target variable (Eq. 6 and Eq. 7; Fig. 3). As a result, in section 3.2 we were able to quantify the average changes in the lower-eye-lid region was 2 mm, which was 15.6% explained by the PAE ( $r = 0.156$ ; Table 3, Fig. 4). Hence, with above-mentioned advantages, the proposed feature visualization and confounding correction approach provides additional insight into the complex association beyond the existing methods (Fig. S3), and may aid clinical and epidemiological researchers in investigating the underlying mechanism of the associations.

To enable the proposed reconstruction-based feature visualization, a low reconstruction error between the input and reconstructed images is required. Therefore, we proposed a different strategy than purging the confounder information from the latent space, that most existing works [9,10,11,12,13,14] use. The

purging of confounder-related information from the latent space can harm the image reconstruction quality [19], since these two optimization objectives can be contradictory: the image reconstruction aims to keep as much information as possible in the latent space (e.g., age information in reconstructing brain images), while the confounder mitigation aims to remove all confounder-related information. This contradiction is even more prominent in case of multiple confounders. The proposed strategy therefore preserves the confounder-related information in the latent space, while circumventing the mentioned problem by finding an alternative confounder-free representation of the imaging data through vector orthogonalization. This enables an optimal trade-off between the image reconstruction quality and the confounder mitigation

The proposed method supports semi-supervised learning (SSL), which has added value in medical image analysis, where labels are often missing or not acceptable to use because of their suboptimal quality. While we expected SLL to improve the image quality for feature interpretation as well as the discriminative capacity of the latent features by using additional imaging data, we only find this for the facial data (Table S3) but not the brain MRI data (Table S4) application. The reconstruction quality (L1-norm and NCC) was similar between the fully supervised and semi-supervised learning setting. This may be due to the fact that our fully supervised brain autoencoder was optimized using a sufficient amount of labelled data, and thus, additional missing-label images could not further improve the optimization of the brain autoencoder.

Our method showcases flexibility, accommodating various data structures, as evidenced by its compatibility with 2D RGB images, 3D meshes, and high-resolution 3D volumetric images. We anticipate that this adaptability will span other image domains that are compatible with autoencoder-based encoding and decoding.

A limitation of the proposed method is that it requires human prior knowledge for the identification of confounders. In the future, we will consider integrating techniques from causal inference [57] with the proposed method for the automatic identification of potential confounders. In addition, while our reconstruction-based feature interpretation technique presumes a continuous latent space, it's worth noting that if faced with input data that has a discrete distribution, this constraint can potentially be overcome using variational autoencoders. These specifically enforce a Gaussian distribution within the latent space.

In conclusion, our AI method, complemented by its semi-supervised variant, offers a promising toolset for enhancing association analysis in medical imaging. Future research can further refine and extend this method, ensuring more robust and interpretable findings in medical imaging studies.

---

## Methods

### 2.1 Datasets

*Simulated 2D solid circles:* We simulated a dataset of 2D images (N=8,000; matrix size 64x64) with black background and greyscale solid circles of different brightness and radius, which we use as input images. To simulate the research scenario of one learning target variable and one confounder variable, we used the brightness of the circle as the learning target and radius as confounder [53]. The brightness (range: 0-1 rescaled from 128-255 in grayscale; mean:  $0.470 \pm 0.135$ ) and radius (range: 3-30 pixels; mean:  $16 \pm 6.320$  pixels) followed a multivariate Gaussian distribution, and the Pearson correlation coefficient between them is -0.668. The center of all circles lies in the geometric center of the image. A brightness of 0 indicates gray and a brightness of 1 indicates white. Details about the datasets is provided in Fig. S1.

*Facial shape dataset:* 3D facial shape imaging data from the multi-ethnic population-based Generation R cohort study is included (mean age: 9.8 years; N=5011) [47]. We built the raw data acquired from a 3dMD (Atlanta (GA), USA) camera system into a template-based dataset [54]. Additionally, phenotyping regarding sex, BMI, ethnicity, low to moderate maternal alcohol exposure during pregnancy, maternal age, and maternal smoking during pregnancy was performed. The binary phenotypes were digitized, namely, Sex: 1 for female and 0 for male; Ethnicity: 1 for Western and 0 for non-Western; Maternal alcohol consumption: 1 for exposed and 0 for non-exposed; Maternal smoking: 1 for exposed and 0 for non-exposed. We evaluate the applicability of the method in a clinical practice setting which examine the association between low-to-moderate prenatal alcohol exposure and children's facial shape. We consider maternal alcohol consumption as the learning target, and as suggested [51,55], include sex, ethnicity, BMI, maternal age, and smoking as confounders, resulting in N=1,515 *labelled samples* (760 non-exposed and 755 exposed) and N=3,496 *missing-label samples*. Details about data characteristic are shown in Table 2, where maternal smoking, maternal age, child BMI, and especially ethnicity showed imbalanced distribution between the non-exposed and exposed groups. The Western group had the highest proportion of different characteristics, accounting for about 48% of the non-exposed group, while above 88% of the exposed groups. Children BMI in the non-exposed group (mean  $18.6 \pm SD 3.2$ ) is overall higher than that in the exposed group (mean  $16.8 \pm SD 2.0$ ).

*Ageing brain dataset:* The Rotterdam Study is a prospective population-based study targeting causes and consequences of age-related diseases among 14,926 participants [26]. In this work, we included 11,801 3D T1-weighted brain MRI scans from N=5,717 participants (mean age:  $64.7 \pm 9.8$  years, female: 54.5%) who have no prevalent dementia or stroke at time of MRI. Scans were acquired on one 1.5T MRI scanner (GE Signa Excite; GE Healthcare, Madison, USA). For 3D T1-weighted images, the acquisition parameters were: TR/TE=13.8ms/2.8ms; imaging matrix of 416x256 in an FOV of 250x250mm<sup>2</sup> [27]. The voxel size was 0.5x0.5x0.8mm<sup>3</sup>. We computed modulated grey matter (GM) maps using voxel-based morphometry (VBM) that describe the local GM density [28, 29]. The matrix size of the resulting modulated GM maps, that we use as input images for the association analysis, is 160x192x144. As the learning target, we use a general cognitive factor (g-factor) that was computed using principal component analysis incorporating color-word interference subtask of the Stroop test, LDST, verbal fluency test, delayed recall score of the 15-WLT, DOT and Purdue pegboard test [56]. Scans acquired at baseline time-point and with available

phenotypes and valid cognitive test results were considered as *labeled samples* (N=2395), which were split into five folds for cross-validation. Additionally, follow-up scans or scans with missing labels were used as *missing-label samples* (N=9,406), and the scans from the same participant were in the same fold.

## 2.2 Methodology

### *Confounders in a geometric prospective in the latent space*

The latent space of an autoencoder can be considered as a vector subspace of  $\mathbb{R}^n$  ( $n$  latent dimensions of the latent space) with basis vectors<sup>1</sup>  $\vec{z}_j$  ( $j=1,2,\dots,n$ ), in which any vector can be represented by  $\vec{r} = [r_1, r_2, \dots, r_n]$  as a linear combination of the basis vectors (Fig. 1(a)). In latent space there exists a vector direction that predominantly captures the relationship between input images and a variable in the dataset (e.g., the learning target, confounders) [24]. By sampling along this vector, a sequence of images can be reconstructed to explain the association between the input images and the variable, and thus we refer to such vectors as *variable-related vectors*. We assume there exist variable-related vectors  $\vec{t} = [t_1, t_2, \dots, t_n]$  and  $\vec{c} = [c_1, c_2, \dots, c_n]$  that represent the learning target  $\mathbf{t}^N$  (N samples) and a confounder  $\mathbf{c}^N$  in the latent space. The confounding issues in this case would be that there is a correlation between  $\vec{t}$  and  $\vec{c}$ , and therefore, the association that  $\vec{t}$  explains between the input images and  $\mathbf{t}$  is confounded by  $\mathbf{c}$ .

To mitigate this confounding effect in the latent space, we aim to find an alternative vector  $\vec{p}^* = [p_1, p_2, \dots, p_n]$  that is independent to  $\vec{c}$  while maximally correlated with  $\vec{t}$ , such that the vector  $\vec{p}^*$  explains the correlation between the input images and  $\mathbf{t}$ , without being confounded by  $\mathbf{c}$ . We refer to  $\vec{p}^*$  as a *confounder-free vector*. A  $\vec{p}^*$  independent to  $\vec{c}$  can be any vector on the plane O that is orthogonal to  $\vec{c}$ . With this constraint, the correlation between  $\vec{p}^*$  and  $\vec{t}$  reaches the maximum if and only if  $\vec{p}^*$  is collinear with the vector projection of  $\vec{t}$  onto the plane O (Fig. 1(a)). To solve this geometric orthogonalization problem and to determine  $\vec{p}^*$  we propose a statistics-based solution in two steps:

1. Given an input image, its latent representation  $\mathbf{d}^n = (d_1, d_2, \dots, d_n)$  can be computed via the encoder, and shown as a datapoint in the latent space (Fig. 1(a)). Subsequently, we calculate  $z_p^* = [d_1, d_2, \dots, d_n] \cdot [p_1, p_2, \dots, p_n] / \|\vec{p}^*\| = (p_1 d_1 + p_2 d_2 + \dots + p_n d_n) / \|\vec{p}^*\|$  as the distance between  $\mathbf{d}'$  and the origin, where  $\mathbf{d}'$  is the point projection of  $\mathbf{d}$  onto  $\vec{p}^*$  (Fig. 1(a)). Therefore, the relationship between input images and  $z_p^*$  is captured by  $\vec{p}^*$ . We refer to  $z_p^*$  as a *confounder-free representation* of its input image.
2. To solve  $\vec{p}^*$ , we perform maximum a posteriori estimation using a statistics-based correlation loss term (Eq. 3). The correlation loss iteratively enforces the parameters  $[p_1, p_2, \dots, p_n]$  to approach the optimal value that minimizes the correlation between  $\mathbf{z}_p^{*N}$  and  $\mathbf{c}^N$ , and maximizes the correlation between  $\mathbf{z}_p^{*N}$  and  $\mathbf{t}^N$  over the dataset. Since the Pearson's correlation coefficient ( $r(\cdot)$ ) equals the cosine value between the two vectors, i.e.,  $r(\mathbf{z}_p^{*N}, \mathbf{c}^N) = \cos\langle \vec{p}^*, \vec{c} \rangle$  [17,18], the optimization of correlations will

---

<sup>1</sup> Non-orthogonal basis vectors.



drive the search of vector  $\vec{p}^*$ . Besides, from Fig. 1(a) it can be inferred that there exists an upper bound for the optimization:

$$|r(\mathbf{z}_p^*, \mathbf{t})| \leq \sqrt{1 - r^2(\mathbf{t}, \mathbf{c})}, \quad s. t. \quad r(\mathbf{z}_p^*, \mathbf{c}) = 0. \quad (1)$$

The proposed statistics-based correlation loss has several advantages, compared with an existing QR - factorization approach [24] for vector orthogonalization. An important one is that it not only estimates  $\vec{p}^*$ , but also encourages the encoder to extract latent features that are linearly correlated to the learning target. Without this correlation loss, the linear correlation between latent features and the learning target could not be guaranteed (Fig. S2 in supplementary). In addition, it can be easily applied to cases with multiple ( $m$ ) confounders (Eq. 4).

### Neural network and loss functions

We implement the proposed algorithm in an autoencoder framework, consisting of an encoder, a decoder, and a projection estimator (Fig. 1(c)). The autoencoder takes  $N$  images  $\mathbf{X}^N$  as input, and outputs the reconstructed images  $\mathbf{X}'^N$  from the latent representations  $\mathbf{D}^{N \times n} = [\mathbf{d}_1^n, \mathbf{d}_2^n, \dots, \mathbf{d}_n^n]$ . By maximizing the structural and intensity similarities between  $\mathbf{X}^N$  and  $\mathbf{X}'^N$ , we expect essential information of  $\mathbf{X}^N$  to be well preserved by  $\mathbf{D}^{N \times n}$  [25]. We optimize this objective using a reconstruction loss term ( $L_{rec}$ ), as measured by the normalized cross correlation (NCC), and the mean absolute error (MAE) between the intensities of  $\mathbf{X}^N$  and  $\mathbf{X}'^N$ :

$$L_{rec}(\mathbf{X}^N, \mathbf{X}'^N) = -\text{NCC}(\mathbf{X}^N, \mathbf{X}'^N) + \text{MAE}(\mathbf{X}^N, \mathbf{X}'^N). \quad (2)$$

Subsequently, we estimate  $\vec{p}^* = [p_1, p_2, \dots, p_n]$  in an a-posteriori manner by formulating it into a trainable linear layer within the autoencoder, which is denoted as a projection estimator. The optimal  $\vec{p}^*$ , and therefore  $\mathbf{z}_p^{*N}$ , is found by optimizing the proposed correlation loss term ( $L_{corr}$ ), which is defined as:

$$L_{corr}(\mathbf{t}^N, \mathbf{c}^N, \mathbf{z}_p^{*N}) = -|r(\mathbf{z}_p^{*N}, \mathbf{t}^N)| + \eta|r(\mathbf{z}_p^{*N}, \mathbf{c}^N)|, \quad (3)$$

where  $|r(\cdot)|$  is the absolute value of the Pearson correlation coefficient;  $\eta$  can be considered as a Lagrange multiplier to weight the correlations. An  $\eta > 1$  tends to minimize  $r(\mathbf{z}_p^{*N}, \mathbf{c}^N)$  to 0 and it enforces a greater correction for confounders, while an  $\eta = 0$  indicates no correction for confounders.  $L_{corr}$  is calculated over a batch of samples. It handles both categorical and continuous confounders. For categorical variables,  $\mathbf{c}^N$  can be converted into dummy variables. For tasks with multiple confounders  $\mathbf{c}_i^N$  ( $i = 1, 2, \dots, m$ ), we propose  $L_{corr}$  as:

$$L_{corr}(\mathbf{t}, \mathbf{c}_1, \mathbf{c}_2, \dots, \mathbf{c}_m, \mathbf{z}_p^*) = -|r(\mathbf{z}_p^*, \mathbf{t})| + \eta(|r(\mathbf{z}_p^*, \mathbf{c}_1)| + \dots + |r(\mathbf{z}_p^*, \mathbf{c}_m)|). \quad (4)$$

Combining objectives of Eq. 2 and 3, we optimize the entire framework using a multi-task loss function ( $L_{joint}$ ):

$$L_{joint} = L_{rec} + \lambda L_{corr}, \quad (5)$$

where  $\lambda$  scales the magnitude of the reconstruction and the correlation terms.

For the tuning of hyperparameters, we prioritize the correlation loss term when adjusting the value of  $\lambda$  (Eq. 5). We suggest a larger batch size ( $>8$ ) since the correlation was computed on a batch level (Eq. 3). To successfully mitigate the confounding effect, we suggest an  $\eta > 2$  (Eq. 3). An  $\eta = 0$  indicates the proposed method without correction for confounders. By comparing the results of  $\eta > 1$  and  $\eta = 0$ , we compared the difference between with and without correction for confounders. To better distinguish them, we refer  $\vec{p}$  and  $z_p$  to the results without correction for confounders ( $\eta = 0$ ), while referring  $\vec{p}^*$  and  $z_p^*$  to those with correction ( $\eta > 1$ ). Detailed settings of the hyperparameters used in our experiments is provided in the supplementary materials.

In addition, since for medical applications often (learning target and confounding) variables are only available for part of the dataset, we provide a semi-supervised implementation of the loss function to fully exploit the available data [**Algorithm 1** in Supplementary], and focus on the results of the semi-supervised setting.

### *Semantic feature visualization*

After optimization of the framework, the parameters of the encoder, decoder, and projection estimator are determined; the confounder-free representation ( $z_p^*$ ) for each given image can be immediately inferred, and used for confounder-free prediction of the learning target ( $t$ ) using logistic or linear regression (LR), i.e.,  $\hat{t} = \text{LR}(z_p^*)$ . To provide insight into the effect of confounder-free association on extracting imaging features, we sample along the confounder-free vector  $\vec{p}^*$  and reconstruct a sequence of images ( $X'_i$ ) that correspond with the predicted target variable  $\hat{t}$ . As formulated in Eq. 6 and Eq. 7, we use the average latent representation  $\vec{d} = (\vec{d}_1, \vec{d}_2, \dots, \vec{d}_n)$  over the testing set as the reference point for the sampling, and consider  $k_i$  as a self-defined parameter to control the step and the range of the sampling and to approach the desired target variable:

$$\hat{t}_i = \text{LR}(\text{PE}(\vec{d} + k_i \vec{p}^*)), \quad i=1, 2, \dots, h, \text{ and} \quad (6)$$

$$X'_i = \text{DEC}(\vec{d} + k_i \vec{p}^*). \quad (7)$$

In the present study, the range of sampling was set to mean  $\pm 3$ \*standard deviation (SD) for experiment 3.1, and mean  $\pm$  SD for experiment 3.2 and 3.3. We set to  $h=11$  and thus generated eleven frames of image for feature interpretation. The difference between the first and the last frame was generated as a heatmap for experiment 3.2 and 3.3. Notably, when sampling along  $\vec{p}^*$ ,  $z_p^*$  changes and this change is correlated to the changes in the learning target ( $\vec{t}$ ) and the reconstructed image ( $X'_i$ ), but invariant to the confounder ( $\vec{c}$ ) (Fig. 1(a)).

### **Data and code availability**

The synthetic data set used in section 3.1, and scripts for all experiments are available at [https://gitlab.com/radiology/comppopbio/ai\\_based\\_association\\_analysis](https://gitlab.com/radiology/comppopbio/ai_based_association_analysis).

## **Acknowledgements**

The Generation R Study is conducted by the Erasmus MC in close collaboration with the School of Law and Faculty of Social Sciences of the Erasmus University Rotterdam, the Municipal Health Service Rotterdam area, Rotterdam, the Rotterdam Homecare Foundation, Rotterdam, and the Stichting Trombosedienst & Artsenlaboratorium Rijnmond (STAR-MDC), Rotterdam. We gratefully acknowledge the contribution of children and parents, general practitioners, hospitals, midwives, and pharmacies in Rotterdam.

The Rotterdam Study is funded by the Erasmus Medical Center and Erasmus University, Rotterdam, Netherlands Organization for the Health Research and Development (ZonMw), the Research Institute for Diseases in the Elderly, the Ministry of Education, Culture and Science, the Ministry for Health, Welfare and Sports, the European Commission (Directorate-General XII), and the Municipality of Rotterdam. The authors are grateful to the study participants, the staff from the Rotterdam Study, and the participating general practitioners and pharmacists.

## **Author contributions**

All authors made significant contributions to this scientific work and approved the final version of the manuscript. X.L. and B.L. were involved in the conception and design of the study, conducted the method development and experiments, and wrote the article. E.E.B. and G.V.R. were involved in the conception and design of the study, supervised the method development and design of experiments, and co-wrote the article. M.W.V. and E.B.W. were involved in the conception and design of the study, reviewed the manuscript, and provided consultation regarding the analysis and interpretation of the data.

## References

(allow up to 70 references)

- [1] Schölkopf, Bernhard, et al. *Elements of Causal Inference: Foundations and Learning Algorithms*. MIT Press, 2017.
- [2] Stewart, Antony. *Basic Statistics and Epidemiology: A Practical Guide, Fourth Edition*. Taylor & Francis Group, 2018. Accessed 9 June 2022.
- [3] *Statistics Applied to Clinical Trials*, edited by Toine F. Cleophas, et al., Springer Netherlands, 2008. Accessed 9 June 2022.
- [4] Vellido, A. "The importance of interpretability and visualization in machine learning for applications in medicine and health care." *Neural Comput & Applic*, vol. 32, 2020, pp. 18069–18083.
- [5] Holm, Elizabeth A. "In defense of the black box." *Science*, vol. 364, no. 6435, 2019, pp. 26-27.
- [6] Adeli, Ehsan. "Chained regularization for identifying brain patterns specific to HIV infection." *NeuroImage*, vol. 183, 2018, pp. 425-437.
- [7] Pourhoseingholi, Mohamad Amin. "How to control confounding effects by statistical analysis." *Gastroenterol Hepatol Bed Bench*, vol. 5, no. 2, 2012, pp. 79–83.
- [8] Koikkalainen, Juha. "Improved Classification of Alzheimer's Disease Data via Removal of Nuisance Variability." *PLOS ONE*, vol. 7, no. 2, 2012, p. e31112.
- [9] Edwards, H. "Censoring Representations with an Adversary." *In: ICLR*, 2016.
- [10] Xie, Q. "Controllable invariance through adversarial feature learning." *In: NIPS*, 2017.
- [11] Zhang, B. "Mitigating unwanted biases with adversarial learning." *In: AIES*, 2018.
- [12] Zhao, Qingyu. "Training confounder-free deep learning models for medical applications." *Nature Communications*, vol. 11, no. 6010, 2020.
- [13] Louizos, Christos. "The Variational Fair Autoencoder." *In: ICLR*, 2016.
- [14] Alemi, A. A. "Deep Variational Information Bottleneck." *In: ICLR*, 2017.
- [15] Creager, E. "Flexibly Fair Representation Learning by Disentanglement." *In: ICML*, 2019.
- [16] Selvaraju, R. R. "Grad-CAM: Visual Explanations from Deep Networks via Gradient-Based Localization." *Int J Comput Vis*, vol. 128, 2019, pp. 336–359.

- [17] Marks, Edmond. "A Note on a Geometric Interpretation of the Correlation Coefficient." *Journal of Educational Statistics*, vol. 7, no. 3, 1982, pp. 233-237.
- [18] Gniadzowski, Zenon. "Geometric interpretation of a correlation." *Zeszyty Naukowe Warszawskiej Wyższej Szkoły Informatyki*, vol. 9, no. 7, 2013, pp. 27-35.
- [19] Liu, X. "Projection-Wise Disentangling for Fair and Interpretable Representation Learning: Application to 3D Facial Shape Analysis." *In: MICCAI*, 2021.
- [20] Xie, Qizhe. "Controllable invariance through adversarial feature learning." *In: NIPS*, 2017.
- [21] Akuzawa, Kei. "Adversarial Invariant Feature Learning with Accuracy Constraint for Domain Generalization." *In: ECML PKDD*, 2019.
- [22] Lee, Jungsoo. "Learning Debaised Representation via Disentangled Feature Augmentation." *In: NIPS*, 2021.
- [23] Kim, Eungyeup. "BiaSwap: Removing Dataset Bias with Bias-Tailored Swapping Augmentation." *In: ICCV*, 2021.
- [24] Balakrishnan, G. "Towards Causal Benchmarking of Bias in Face Analysis Algorithms." *In: ECCV*, 2020.
- [25] Li, B., Liu, X., Niessen, W., et al. "A high-resolution autoencoder for construction of interpretable brain MRI endophenotypes." *In: annual meeting of Organization of Human Brain Mapping (OHBM) 2022*.
- [26] M.A. Ikram, G. Brusselle, M. Ghanbari, A. Goedegebure, M.K. Ikram, M. Kavousi, B.C. Kieboom, C.C. Klaver, R.J. de Knecht, A.I. Luik, et al. "Objectives, design and main findings until 2020 from the Rotterdam study." *Eur. J. Epidemiol.* (2020), pp. 1-35.
- [27] M.A. Ikram, A. van der Lugt, W.J. Niessen, G.P. Krestin, P.J. Koudstaal, A. Hofman, M.M. Breteler, M.W. Vernooij. "The Rotterdam scan study: design and update up to 2012." *Eur. J. Epidemiol.*, 26 (10) (2011), pp. 811-824.
- [28] Good CD, Johnsrude IS, Ashburner J, Henson RN, Friston KJ, Frackowiak RS. "A voxel-based morphometric study of ageing in 465 normal adult human brains." *Neuroimage*. 2001 Jul; 14(1 Pt 1):21-36.
- [29] Roshchupkin GV, Adams HH, van der Lee SJ, Vernooij MW, van Duijn CM, Uitterlinden AG, van der Lugt A, Hofman A, Niessen WJ, Ikram MA. "Fine-mapping the effects of Alzheimer's disease risk loci on brain morphology." *Neurobiol Aging*. 2016 Dec; 48():204-211.
- [30] Shen D., Wu G., Suk H. "Deep Learning in Medical Image Analysis." *Annual Review of Biomedical Engineering*. 2017. (19):221-248
- [31] Jooheon Sung, John L Hopper, Co-evolution of epidemiology and artificial intelligence: challenges and opportunities, *International Journal of Epidemiology*, 2023;; dyad089, <https://doi.org/10.1093/ije/dyad089>
- [32] Fan FL, Xiong J, Li M, Wang G. On Interpretability of Artificial Neural Networks: A Survey. *IEEE Trans Radiat Plasma Med Sci*. 2021 Nov;5(6):741-760. doi: 10.1109/trpms.2021.3066428. Epub 2021 Mar 17. PMID: 35573928; PMCID: PMC9105427.

- [33] Selvaraju, R.R., Cogswell, M., Das, A. et al. Grad-CAM: Visual Explanations from Deep Networks via Gradient-Based Localization. *Int J Comput Vis* 128, 336–359 (2020). <https://doi.org/10.1007/s11263-019-01228-7>
- [34] Lundberg, Scott and Lee, Su-In. "A unified approach to interpreting model predictions" In *NIPS* (2017)
- [35] Grégoire Montavon, Sebastian Lapuschkin, Alexander Binder, Wojciech Samek, Klaus-Robert Müller, Explaining nonlinear classification decisions with deep Taylor decomposition, *Pattern Recognition*, Volume 65, 2017, Pages 211-222
- [36] Bach S, Binder A, Montavon G, Klauschen F, Müller KR, Samek W. On Pixel-Wise Explanations for Non-Linear Classifier Decisions by Layer-Wise Relevance Propagation. *pLoS One*. 2015 Jul 10;10(7):e0130140. doi: 10.1371/journal.pone.0130140. PMID: 26161953; PMCID: PMC4498753.
- [37] X. Chen, Y. Duan, R. Houthoofd, J. Schulman, I. Sutskever, and P. Abbeel, "InfoGAN: Interpretable representation learning by information maximizing generative adversarial nets," in *Proc. NeurIPS*, 2016, pp. 2172–2180.
- [38] A. Stone, H. Wang, M. Stark, Y. Liu, D. S. Phoenix, and D. George, "Teaching compositionality to CNNs," in *Proc. CVPR*, 2017, pp. 5058–5067.
- [39] Zhao Q., Adeli E., Honnorat N., Leng T., Pohl K. M.: Variational AutoEncoder for Regression: Application to Brain Aging Analysis. In: *MICCAI* (2019)
- [40] Mandy Lu, Qingyu Zhao, Jiequan Zhang, Kilian M. Pohl, Li Fei-Fei, Juan Carlos Niebles, Ehsan Adeli. Metadata Normalization In: *CVPR* (2021)
- [41] Vento, A., Zhao, Q., Paul, R., Pohl, K.M., Adeli, E. (2022). A Penalty Approach for Normalizing Feature Distributions to Build Confounder-Free Models. In: Wang, L., Dou, Q., Fletcher, P.T., Speidel, S., Li, S. (eds) *Medical Image Computing and Computer Assisted Intervention – MICCAI 2022*. *MICCAI 2022. Lecture Notes in Computer Science*, vol 13433. Springer, Cham. [https://doi.org/10.1007/978-3-031-16437-8\\_37](https://doi.org/10.1007/978-3-031-16437-8_37)
- [42] Sarhan, M.H., Navab, N., Eslami, A., Albarqouni, S. (2020). Fairness by Learning Orthogonal Disentangled Representations. In: Vedaldi, A., Bischof, H., Brox, T., Frahm, JM. (eds) *Computer Vision – ECCV 2020*. *ECCV 2020. Lecture Notes in Computer Science()*, vol 12374. Springer, Cham. [https://doi.org/10.1007/978-3-030-58526-6\\_44](https://doi.org/10.1007/978-3-030-58526-6_44)
- [43] Tartaglione, E., Barbano, C.A., Grangetto, M.: End: entangling and disentangling deep representations for bias correction. In: *Proceedings of the IEEE/CVF Conference on Computer Vision and Pattern Recognition*, pp. 13508–13517 (2021)
- [44] X. Hou, L. Shen, K. Sun and G. Qiu, "Deep Feature Consistent Variational Autoencoder" 2017 IEEE Winter Conference on Applications of Computer Vision (WACV), Santa Rosa, CA, USA, 2017, pp. 1133-1141, doi: 10.1109/WACV.2017.131.
- [45] Gong S., Chen L., Bronstein M. and Zafeiriou S.: SpiralNet++: A Fast and Highly Efficient Mesh Convolution Operator. In: *ICCVW* (2019)

- [46] Jones KL, Smith DW. Recognition of the fetal alcohol syndrome in early pregnancy. *Lancet* 1973;ii:999–1001.
- [47] Jaddoe VWV, Mackenbach JP, Moll HA, Steegers EAP, Tiemeier H, Verhulst FC, Witteman JCM, Hofman A. The Generation R Study: study design and cohort profile. *Eur J Epidemiol* 2006;21:475–484.
- [48] Zhang, M., Wu, S., Du, S. et al. Genetic variants underlying differences in facial morphology in East Asian and European populations. *Nat Genet* 54, 403–411 (2022). <https://doi.org/10.1038/s41588-022-01038-7>
- [49] Franciscus, R.G. and Long, J.C. (1991), Variation in human nasal height and breadth. *Am. J. Phys. Anthropol.*, 85: 419-427. <https://doi.org/10.1002/ajpa.1330850406>
- [50] Min Jiang, Yuanyuan Shang, Guodong Guo, On visual BMI analysis from facial images, *Image and Vision Computing*, Volume 89, 2019, Pages 183-196
- [51] Muggli E, Matthews H, Penington A, Claes P, O'Leary C, Forster D, Donath S, Anderson PJ, Lewis S, Nagle C, Craig JM, White SM, Elliott EJ, Halliday J. Association Between Prenatal Alcohol Exposure and Craniofacial Shape of Children at 12 Months of Age. *JAMA Pediatr.* 2017 Aug 1;171(8):771-780. doi: 10.1001/jamapediatrics.2017.0778.
- [52] H. Eugene Hoyme, Wendy O. Kalberg, Amy J. Elliott, Jason Blankenship, David Buckley, Anna-Susan Marais, Melanie A. Manning, Luther K. Robinson, Margaret P. Adam, Omar Abdul-Rahman, Tamison Jewett, Claire D. Coles, Christina Chambers, Kenneth L. Jones, Colleen M. Adnams, Prachi E. Shah, Edward P. Riley, Michael E. Charness, Kenneth R. Warren, Philip A. May; Updated Clinical Guidelines for Diagnosing Fetal Alcohol Spectrum Disorders. *Pediatrics* August 2016; 138 (2): e20154256. 10.1542/peds.2015-4256
- [53] Github. [https://github.com/tsingmessage/projection\\_wise\\_disentangling\\_FRL](https://github.com/tsingmessage/projection_wise_disentangling_FRL).
- [54] X Liu and others, Association between prenatal alcohol exposure and children's facial shape: a prospective population-based cohort study, *Human Reproduction*, Volume 38, Issue 5, May 2023, Pages 961–972, <https://doi.org/10.1093/humrep/dead006>
- [55] Howe LJ, Sharp GC, Hemani G, Zuccolo L, Richmond S, Lewis SJ. Prenatal alcohol exposure and facial morphology in a UK cohort. *Drug Alcohol Depend* 2019;197:42–47.
- [56] Hoogendam, Y.Y., Hofman, A., van der Geest, J.N. et al. Patterns of cognitive function in aging: the Rotterdam Study. *Eur J Epidemiol* 29, 133–140 (2014). <https://doi.org/10.1007/s10654-014-9885-4>
- [57] Gao, T. & Ji, Q. Local causal discovery of direct causes and effects. in *Advances in Neural Information Processing Systems*, (eds Cortes, C., Lawrence, N., Lee, D., Sugiyama, M. & Garnett, R.) 512–2520 (2015).
- [58] Roshchupkin, G.V., Zonneveld, H.I., Adams, H.H.H., Vernooij, M.W., Niessen, W.J. and Ikram, M.A. (2016), O3-03-06: Grey Matter Density in Relation to Cognitive Function. *Alzheimer's & Dementia*, 12: P288-P288. <https://doi.org/10.1016/j.jalz.2016.06.523>

# AI-based association analysis for medical imaging using latent-space geometric confounder correction

Xianjing Liu<sup>1,2\*</sup>, Bo Li<sup>1\*</sup>, Meike W. Vernooij<sup>1,3</sup>, Eppo B. Wolvius<sup>2</sup>, Gennady V. Roshchupkin<sup>1,3#</sup>, Esther E. Bron<sup>1#</sup>

<sup>1</sup>Dept. of Radiology & Nuclear Medicine, Erasmus University Medical Center, Rotterdam, the Netherlands

<sup>2</sup>Dept. of Oral and Maxillofacial Surgery, Erasmus University Medical Center, Rotterdam, the Netherlands

<sup>3</sup>Dept. of Epidemiology, Erasmus University Medical Center, Rotterdam, the Netherlands

\*,# These authors contributed equally to this work.

## supplementary



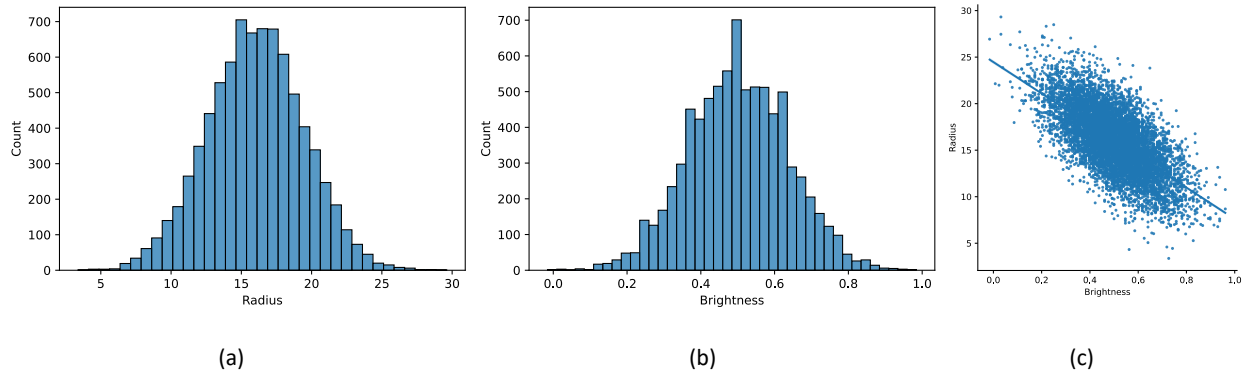
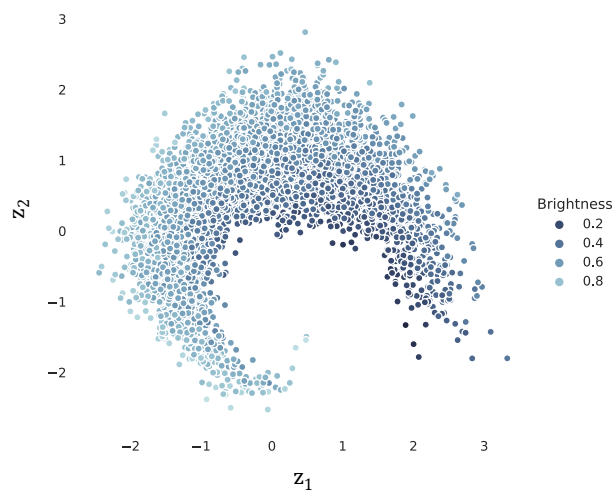
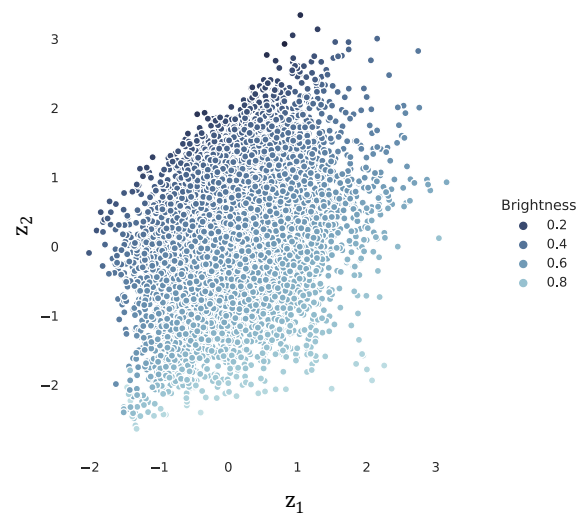


**Fig. S1:** Data characteristic of the data set used in experiment 3.1. **(a)** Histogram distribution of circle radius; **(b)** Histogram distribution of circle brightness; **(c)** Multivariate Gaussian distribution of radius and brightness.



(a) latent space trained in an unsupervised manner;



(b) latent space trained in a supervised manner (Eq. 5)

**Fig. S2:** Distribution of datapoints in the 2-D latent space in experiment 3.1. **(a)** the autoencoder was optimized only with the reconstruction loss, and the brightness was non-linearly captured in the latent space; **(b)** the autoencoder was optimized with the reconstruction loss and the correlation loss (Eq. 5), and the brightness was linearly captured in the latent space.

**Table S1:** Comparison between our method and CF-net [12] in experiment 3.1.

Methods	With or without confounder correction	r-MSE	Pearson's correlation coefficient		Image reconstruction
			$r(\mathbf{z}_p, \text{radius})$	$r(\mathbf{z}_p, \text{brightness})$	L1-norm
Ours	Without ( $\eta = 0$ in Eq. 3)	0.018±0.003	+0.670±0.024	-0.991±0.003	0.0001±0.00004
	With ( $\eta > 1$ in Eq. 3)	0.096±0.004	+0.026±0.006	-0.737±0.011	0.0001±0.00004
CF-net	Without	0.016±0.004	+0.670±0.022	-0.9978±0.002	NA
	With	0.010±0.008	+0.036±0.017	-0.725±0.013	NA

Notion ' $\mathbf{z}_p$ ' here is referring to notion ' $\mathbf{y}$ ' in the CF-net [12] paper.

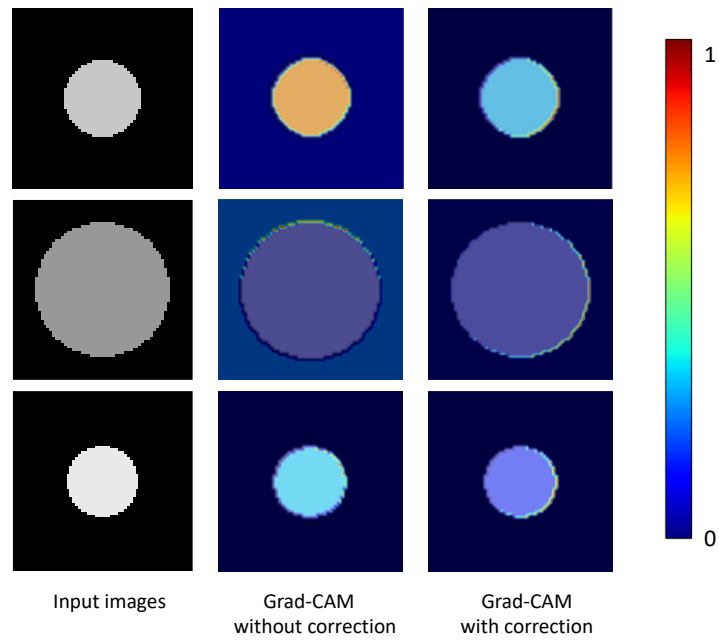


**Fig. S3:** Gram-CAM based feature visualization in CF-Net [ref], for experiment 3.1 where the learning target is circle brightness while the confounder is circle radius. Regions with more red color are more important for the prediction of the learning target.

## Implementation details of the semi-supervised learning (SSL) settings:

In particular, for each training batch, we update the parameters in two steps: 1) update by  $L_{rec}$  based on the unlabeled data (half batch), and 2) update by  $L_{joint}$  based on the labelled data (half batch). A detailed implementation is provided in the supplementary file (Algorithm 1).

---

**Algorithm 1:** proposed semi-supervised fair representation learning

---

**Require:**  $\mathbf{X}^u$  (unlabelled data),  $\mathbf{X}^l$  (labelled data),  $N_{epoch}$ ,  $N_{batch\_size}$

---

**Parameters:**  $\theta_{enc}$ ,  $\theta_{dec}$ ,  $\theta_{pe}$

1.  $N_{sample} = \min \{len(\mathbf{X}^u), len(\mathbf{X}^l)\}$
  2.  $i = 0$
  3. **while**  $i < N_{epoch}$ , **do**:
  4.     randomly sample  $\mathbf{X}^{us}$ ,  $\mathbf{X}^{ls}$  from  $\mathbf{X}^u$ ,  $\mathbf{X}^l$ , respectively.  $len(\mathbf{X}^{us}) = len(\mathbf{X}^{ls}) = N_{sample}$
  5.      $j = 0$
  6.     **while**  $j < N_{sample}$ , **do**:
  7.         Acquire *unlabelled* datapoints  $\mathbf{X}^{ut}$  from  $\mathbf{X}^{us}$ .  $len(\mathbf{X}^{ut}) = N_{batch\_size}/2$
  8.         update  $\theta_{enc}$  and  $\theta_{dec}$  by  $L_{rec}(\mathbf{X}^{ut})$
  9.         Acquire *labelled* datapoints  $\mathbf{X}^{lt}$  from  $\mathbf{X}^{ls}$ .  $len(\mathbf{X}^{lt}) = N_{batch\_size}/2$
  10.        update  $\theta_{enc}$ ,  $\theta_{dec}$  and  $\theta_{pe}$  by  $L_{joint}(\mathbf{X}^{lt})$
  11.         $j = j + N_{batch\_size}$
  12.     **end while**
  13.      $i = i + 1$
  14. **end while**
  15. **return**  $\theta_{enc}$ ,  $\theta_{dec}$ ,  $\theta_{pe}$
-

**Table S2: Hyperparameter settings for experiments.**

	Experiment 1	Experiment 2	Experiment 3
supervision	Fully supervised	Fully supervised + SSL	Fully supervised + SSL
Data split	5-fold cross-validation	5-fold cross-validation	5-fold cross-validation
$\eta$	2	2	2
$\lambda$	500	2	0.00001
Latent dimension	2	64	64
Batch size	64	64	8
epoch	50	300	300

The value of  $\lambda$  highly depends on the magnitude of L1 loss in the experiment.

**Table S3: Association analysis between PAE (learning target) and children’s facial shape (input image).** Results are presented without and with controlling of confounders (ethnicity, BMI, sex, maternal smoking and maternal age), and for both supervised and semi-supervised learning. The metrics for AUC and PAE are the higher the better, those for ethnicity, BMI, sex, maternal smoking, maternal age and L1-norm are the lower the better.

With or without confounder correction	Semi- or fully supervised	AUC	PAE	Correlation coefficient between $\mathbf{z}_p$ and:					Image reconstruction
				Ethnicity	BMI	Sex	Maternal smoking	Maternal age	L1-norm
without ( $\eta = 0$ in Eq. 3)	Fully	0.731±0.034	+0.400±0.059	+0.310±0.050	-0.334±0.059	+0.050±0.050	+0.100±0.055	+0.226±0.060	0.315±0.006
with ( $\eta > 1$ in Eq. 3)	Fully	0.579±0.028	+0.118±	+0.040±0.017	-0.030±0.018	+0.044±0.042	+0.032±0.031	+0.031±0.018	0.344±0.017
without ( $\eta = 0$ in Eq. 3)	Semi	0.746±0.018	+0.405±0.043	+0.389±0.085	-0.349±0.010	+0.049±0.043	+0.080±0.054	+0.216±0.049	0.294±0.017
with ( $\eta > 1$ in Eq. 3)	Semi	0.592±0.004	+0.156±0.008	+0.064±0.018	-0.040±0.016	+0.043±0.030	+0.026±0.009	+0.028±0.026	0.312±0.015

**Table S4: Association analysis of the learning target global cognition (g-factor) and constructed latent representation of grey matter density map input ( $z_p$ ).** Results are presented without and with controlling of confounders (age, sex, and educational years), and for both supervised and semi-supervised learning. The metrics for g-factor and normalized cross-correlation (NCC) are the higher the better, those for age, sex, educational years, and L1-norm are the lower the better.

Confounders control	Semi- or fully supervised	<u>Correlation coefficient between <math>z_p</math> and:</u>				<u>Image reconstruction quality</u>	
		G-factor $\uparrow$	Age $\downarrow$	Sex $\downarrow$	Educational years $\downarrow$	NCC $\uparrow$	L1-norm $\downarrow$
Without (ref eq) ( $\eta = 0$ in Eq. 3)	Fully	0.48 $\pm$ 0.03	-0.73 $\pm$ 0.01	-0.07 $\pm$ 0.05	0.13 $\pm$ 0.05	0.22 $\pm$ 0.0007	0.09 $\pm$ 0.0003
With (ref eq) ( $\eta > 1$ in Eq. 3)	Fully	0.03 $\pm$ 0.03	-0.04 $\pm$ 0.03	-0.05 $\pm$ 0.02	0.03 $\pm$ 0.04	0.22 $\pm$ 0.0004	0.09 $\pm$ 0.0001
Without ( $\eta = 0$ in Eq. 3)	Semi	0.49 $\pm$ 0.04	-0.73 $\pm$ 0.01	-0.08 $\pm$ 0.03	0.13 $\pm$ 0.05	0.22 $\pm$ 0.0008	0.09 $\pm$ 0.0003
With ( $\eta > 1$ in Eq. 3)	Semi	0.05 $\pm$ 0.04	-0.04 $\pm$ 0.03	-0.03 $\pm$ 0.02	0.06 $\pm$ 0.04	0.22 $\pm$ 0.0010	0.09 $\pm$ 0.0004